

MATERIALS SCIENCE

Acoustophoretic printing

Daniele Foresti^{1*}, Katharina T. Kroll¹, Robert Amissah¹, Francesco Sillani¹, Kimberly A. Homan¹, Dimos Poulikakos², Jennifer A. Lewis^{1*}

Droplet-based printing methods are widely used in applications ranging from biological microarrays to additive manufacturing. However, common approaches, such as inkjet or electrohydrodynamic printing, are well suited only for materials with low viscosity or specific electromagnetic properties, respectively. While in-air acoustophoretic forces are material-independent, they are typically weak and have yet to be harnessed for printing materials. We introduce an acoustophoretic printing method that enables drop-on-demand patterning of a broad range of soft materials, including Newtonian fluids, whose viscosities span more than four orders of magnitude (0.5 to 25,000 mPa·s) and yield stress fluids ($\tau_0 > 50$ Pa). By exploiting the acoustic properties of a subwavelength Fabry-Perot resonator, we have generated an accurate, highly localized acoustophoretic force that can exceed the gravitational force by two orders of magnitude to eject microliter-to-nanoliter volume droplets. The versatility of acoustophoretic printing is demonstrated by patterning food, optical resins, liquid metals, and cell-laden biological matrices in desired motifs.

INTRODUCTION

New methods for mesoscale patterning of soft materials will drive scientific advances in the areas of optics, electronics, biology, and beyond (1). To date, inkjet printing is the most widely used method to controllably generate and pattern droplets. In this technique, drop detachment is governed by the Rayleigh-Plateau instability (2). This dynamic process involves a strong coupling between interfacial and viscous forces, as characterized by a nondimensional number, the Ohnesorge number Oh , and its inverse $Z = Oh^{-1} = (\rho\sigma 2R)^{1/2}/\mu$, where R is the droplet radius, ρ is the density, σ is the surface tension, and μ is the viscosity of the liquid. To ensure successful droplet ejection, the ink composition and printing parameters must be precisely tuned within a narrow printing window $1 < Z < 14$ (2). Hence, despite its high resolution (10- μ m droplets), contactless deposition, and high drop generation rates (1 to 100 kHz) (2), inkjet printing is well suited only for patterning low viscosity inks (roughly 10 to 100 times higher than the viscosity of water). When the fluid viscosity exceeds 1000 mPa·s, one must rely on transfer (that is, jetting) techniques, such as those based on laser-induced forward transfer or valve-based printing, that generate and deposit elongated filamentary jets onto a substrate placed at close proximity to the source film or nozzle (3–6). In these methods, the volumetric transfer rate depends on the material viscosity, source film thickness (or nozzle size), and source-substrate distance. These parameters must be optimized for each ink composition, which is particularly challenging for materials whose physical properties change over time.

To overcome these limitations, one must decouple fluid flow from the droplet detachment process. In the case of a dripping faucet (7, 8), gravity acts as an external body force independent of the nozzle and ink reservoir system so that detachment occurs when the gravitational force $F_g = 4/3\pi R^3 \rho g = V\rho g$, where V is the drop volume and g is the gravitational acceleration, exceeds the opposing capillary force $F_c = \pi\sigma d$ for a given nozzle diameter, d . Notably, this approach allows one to eject fluid droplets of nearly any viscosity, for example, even droplets of pitch

whose viscosity exceeds 10^8 Pa·s (9). To reduce the droplet volume at detachment, $V = \pi\sigma d/\rho g$, one can use an external force ($\gg 1g$) to essentially pull on the pendant drop. One promising method, electrohydrodynamic printing, uses electrical forces to eject droplets at high speed and resolution (10, 11). However, this method requires not only inks with specific electromagnetic properties, but also precise coupling between the nozzle, substrate, and existing printed features to induce the desired electrical field.

Acoustophoretic forces are independent from any electromagnetic properties and have been used to trap or manipulate samples within an acoustic field (12–15). They are typically used in lab-on-a-chip devices to sort and manipulate fine particles, cells, or droplets within a liquid (16–18). In acoustic printing, acoustic waves are focused on a liquid-air interface to eject single droplets (19, 20). It is a nozzle-free method, with great control over size of droplet and ejection frequency. However, drop generation requires the liquid to have properties akin to those needed for inkjet printing. To create droplets, surface acoustic waves have recently been used in microfluidic devices (21, 22). However, their application in air yields limited control over droplet formation, ejection, and deposition when compared to acoustic printing (23, 24). Here, we report a new method, known as acoustophoretic printing, that harnesses the nonlinear acoustic properties of a Fabry-Perot resonator to generate and pattern droplets of materials in air over a wide range of compositions and properties.

RESULTS

Acoustophoretic force

Our resonator consists of a single subwavelength cavity (25), which has been used in alternate geometries to enhance the resolution of acoustic imaging (26, 27) and attract microparticles in a liquid (28). When spherical drops are generated in a standing-wave configuration, they are governed by the following force balance (Fig. 1A)

$$F_c = \pi\sigma d = F_g + F_a = V\rho(g + g_a) \rightarrow V = \pi d\sigma/\rho g_{eq} \quad (1)$$

where the capillary force, $F_c (= \pi\sigma d)$, is opposed by both the gravitational force, F_g , and the acoustophoretic force, $F_a \propto R^3 P^2 \propto V P^2$ (where R is the drop radius and P is the acoustic pressure) (15, 29).

¹John A. Paulson School of Engineering and Applied Sciences, Wyss Institute for Biologically Inspired Engineering, Harvard University, Cambridge, MA 02138, USA.

²Laboratory of Thermodynamics in Emerging Technologies, Department of Mechanical and Process Engineering, ETH Zurich, Sonneggstrasse 3, CH-8092 Zurich, Switzerland.

*Corresponding author. Email: dforesti@seas.harvard.edu (D.F.); jalewis@seas.harvard.edu (J.A.L.)

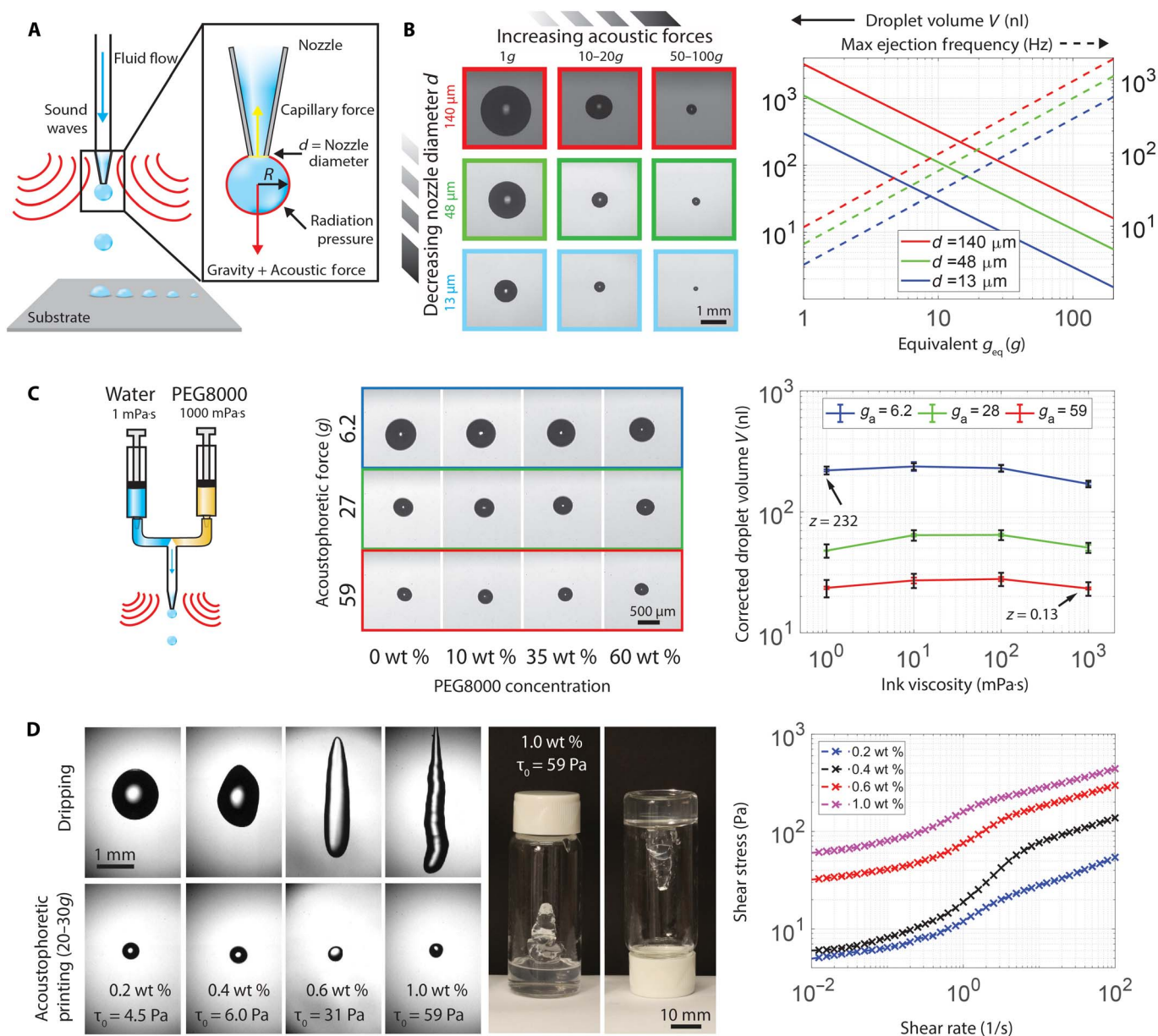


Fig. 1. Acoustophoretic printing. (A) Schematic view of acoustophoretic printing, in which the radiation pressure provides an additional force that aids drop formation and ejection. (B) Optical images of droplets formed as a function of varying acoustophoretic forces and nozzle diameter d (left), images obtained under simple dripping mode (F_g), and log-log plot of droplet volume and maximum ejection frequency over the range of acoustophoretic forces explored (right). (C) Schematic view of a two-component nozzle that delivers a mixture of water and PEG (molecular weight = 8000 g/mol) ranging from 0 to 60 wt % PEG (viscosity between 1 and 1000 mPa-s, respectively) (left), optical images of droplets generated during acoustophoretic printing of these model fluids (middle), and log-log plot of droplet volume as a function of ink viscosity (right, black bars denote 1 pixel = 9 μm). (D) Acoustophoretic printing of prototypical yield stress fluids composed of 0.2 to 1.0 wt % carbopol in water alongside images of an ink vial containing a carbopol solution of 1.0 wt % (left, middle) and log-log plot of shear stress as a function of shear rate for these solutions.

Droplets are ejected from the nozzle during acoustophoretic printing when $F_g + F_a > F_c$, with an effective acoustic acceleration $g_a = ((F_a/F_g) - 1)g$. Because $F_a \propto g_a \propto P^2$, the droplet volume scales as $V \propto 1/P^2$ for any fluid or nozzle (see Materials and Methods). As the acoustophoretic force increases from F_g (simple dripping faucet) to $116F_g$ at a drop density of $\rho \approx 1000 \text{ kg/m}^3$, the drop radius decreases for a given nozzle size, ranging from a maximum value that exceeds 800 μm (F_g , $d = 140 \mu\text{m}$) to less than 65 μm ($116F_g$, $d = 13 \mu\text{m}$) (Fig. 1B and movie S1). When the acoustophoretic force dominates the gravita-

tion force (that is, $F_a > 10F_g$), droplets can be ejected in any direction by rotating the printing platform in space (fig. S1 and movie S2). Concomitantly, the theoretical maximum droplet ejection rate increases linearly up to values of $\sim 10^3$ Hz or higher (Fig. 1B and fig. S2A).

Because the fluid viscosity μ does not appear in Eq. 1, monodisperse droplets can be generated even when the ink composition is varied during the printing process provided that the acoustophoretic pressure and nozzle diameter are held constant. To demonstrate this, we used model fluids composed of aqueous polyethylene solution [polyethylene glycol,

molecular weight 8000 (PEG8000)], whose concentration is varied from 0 to 60 weight % (wt %) PEG during the acoustophoretic printing process. Over this compositional range, the ink viscosity spans three orders of magnitude from μ of 1 mPa·s to 1000 mPa·s, corresponding to $0.13 < Z < 232$. As expected, the effect of fluid viscosity on the ejected droplet volume V is negligible (Fig. 1C). The minor variations observed stem only from the difference in surface tension between pure water and the PEG solutions, which linearly influences V at detachment (Eq. 1 and fig. S2B) (30).

The process of detachment and ejection of highly viscous droplets via acoustophoretic printing is very similar to simple dripping ($F_a = 0$). Acoustophoretic printing of honey (25,000 Pa·s) reveals that a long, thin thread forms, which breaks up when the combined gravitational and acoustophoretic forces exceed the capillary force, that is, $F_g + F_a > F_c$ (fig. S2C and movie S3). In both cases, we observe long threads whose diameter ultimately becomes smaller than the resolution of the camera at breakup. While satellite droplets may form, they would be roughly six to nine orders of magnitude smaller in volume than the primary droplet.

By decoupling fluid flow and droplet detachment, even yield stress fluids, that is, materials that act like solids at rest, yet flow as liquids when the applied shear stress exceeds their shear yield stress ($\tau > \tau_0$), can be ejected as droplets, unlike transfer (jetting) techniques (3–6). For example, droplets of a carbopol-based gel, a prototypical yield stress material, can be acoustophoretically ejected (Fig. 1D). By contrast, these gels form highly elongated, globular objects when subjected to a simple dripping mode ($F = F_g$) using the same nozzle.

Subwavelength acoustophoretic voxel ejector design

To realize the above demonstrations of acoustophoretic printing, we created the subwavelength acoustophoretic voxel ejector (subWAVE) shown in Fig. 2A. Upon validating our design based on the work by Christensen *et al.* (25), we explored the parametric space $H_h - d_h$ of a subwavelength cylindrical cavity. Using a driving ultrasonic frequency of about 25 kHz (corresponding to a wavelength $\lambda = 14$ mm), we selected $H_h = 0.36\lambda = 5.1$ mm and $d_h = 0.14\lambda = 2$ mm within the first Fabry-Perot resonance (Fig. 2A and fig. S3). These dimensions are convenient for realizing the experimental prototype (Fig. 2B), because fluid is delivered through a tapered glass nozzle with a relatively large diameter of 1 mm placed along the central axis of the subWAVE. An emitter on top of the subwavelength cavity induces a subwavelength resonance inside the subWAVE (Materials and Methods). We investigated the acoustophoretic forces within the subWAVE by a combination of finite element method and analytical modeling. Only when the nozzle tip is located within a specific height range inside the subWAVE is the out-coupling required for drop ejection achievable, as highlighted by the green area in Fig. 2C. Figure 2D shows that the vertical force distribution inside the subWAVE is experimentally verified by measuring the ejected droplet size (Materials and Methods). The model captures the physics of drop ejection for our subWAVE, which induces an acoustic field that intrinsically out-couples the detached drop under the requisite conditions (Fig. 2E). The acoustic field is both highly localized, that is, independent of the substrate, and capable of generating a force one to two orders of magnitude higher than a classical acoustic levitator (Fig. 2F and Materials and Methods).

Drop-on-demand printing of synthetic and biological materials

To demonstrate the drop-on-demand capabilities of acoustophoretic printing, we created a rasterized image composed of patterned droplets

(1:1 glycerol-to-water ratio, dyed orange to aid visualization) over a large area (10 cm \times 7.5 cm), with typical print speeds of approximately 1 to 10 mm/s (Fig. 3A). As a preliminary demonstration, we show that three-dimensional (3D) acoustophoretic printing is also possible, in which an aqueous PEG (50 wt % PEG10000 and $\mu = 680$ mPa·s) is patterned into a multilayered H-shape architecture (fig. S4).

The subWAVE strongly confines the highly amplified acoustic field (~ 170 dB) within a fraction of the wavelength with a minimum offset distance of 1 mm from the substrate, equivalent to 0.07λ (Fig. 3, B and C, and fig. S5). Ballistic ejection of individual droplets is confirmed by measuring the exit angle error (Fig. 3C, right axis), which remains nearly constant for different nozzle tip–substrate distances. However, we do find that the drop trajectory accuracy decreases with increasing acoustic force for high acoustophoretic fields ($g_a = 62g$; Fig. 3C). We note that a linear improvement is expected with increasing driving frequency, because the absolute dimensions of the system scale with the acoustic wavelength (31). In addition, for the same acoustic pressure amplitude and droplet diameter, the acoustophoretic force increases linearly with the frequency. While sound waves in air can be strongly attenuated at high frequencies, this can be neglected for frequencies up to 1 MHz in our subWAVE device (32), because the acoustic waves only travel a short distance. To construct a subWAVE that operates at even higher frequencies, one must use higher-precision, microfabrication techniques.

To highlight the broad materials space for acoustophoretic printing, we generated and patterned droplets composed of honey, optical resin, cell-laden hydrogel matrices, and metallic liquid inks, whose collective properties span nearly six orders of magnitude, that is, $10^{-3} < Z < 10^3$ (Fig. 4A). As a simple example, we printed honey ($\mu = 25,000$ mPa·s, $Z = 0.007$) in the form of droplets on a white chocolate bar under ambient conditions (Fig. 4B). This contactless drop deposition method allows any soft substrate to be used, including a cream filling (fig. S6). Next, we created a microlens array inspired by compound eyes (33) by printing droplets composed of an ultraviolet (UV) light-curable, transparent optical adhesive (NOA60; $\mu = 300$ mPa·s, $Z = 0.5$) on both planar and curvilinear substrates (Fig. 4C). Each droplet undergoes modest wetting and spreading to form a nearly hemispherical microlens (contact angle, $74^\circ \pm 4^\circ$).

During acoustophoretic printing, the acoustic waves are mostly reflected ($>99.9\%$) at the droplet surface due to the mismatch in acoustic impedance between air and the fluid ink. Because negligible sonication occurs within each drop, fragile cargo, such as mammalian cells or proteins, can be readily patterned with high viability (29) akin to other droplet or extrusion-based bioprinting techniques (34, 35). Specifically, we demonstrated this by printing a cell-laden ink composed of bone marrow-derived human mesenchymal stem cells (hMSCs; 5×10^5 cells/ml) suspended in a chilled collagen I solution (36, 37) at 5 mg/ml ($\mu = 80$ mPa·s, $Z = 2$; Fig. 4D and fig. S7A) onto hydrophobically modified glass substrates. After printing, the droplets are encapsulated in a secondary hydrogel matrix and cultured in standard stem cell medium (Materials and Methods). On day 1, we observed that hMSCs spread and begin to proliferate within the collagen I matrix in the printed drops ($g_{eq} = 43g$; Fig. 4Da). By day 7, hMSCs are observed to span the entire thickness of the printed droplets (movie S4). To quantify the effects of acoustophoretic printing on cell viability, we dispensed the hMSC-laden collagen I ink into 48-well plates at different acoustophoretic forces. As controls, this ink is also patterned in a simple dripping mode (1g) and manually using a pipette. Notably, hMSCs within the printed drops exhibit high viability compared to pipetted

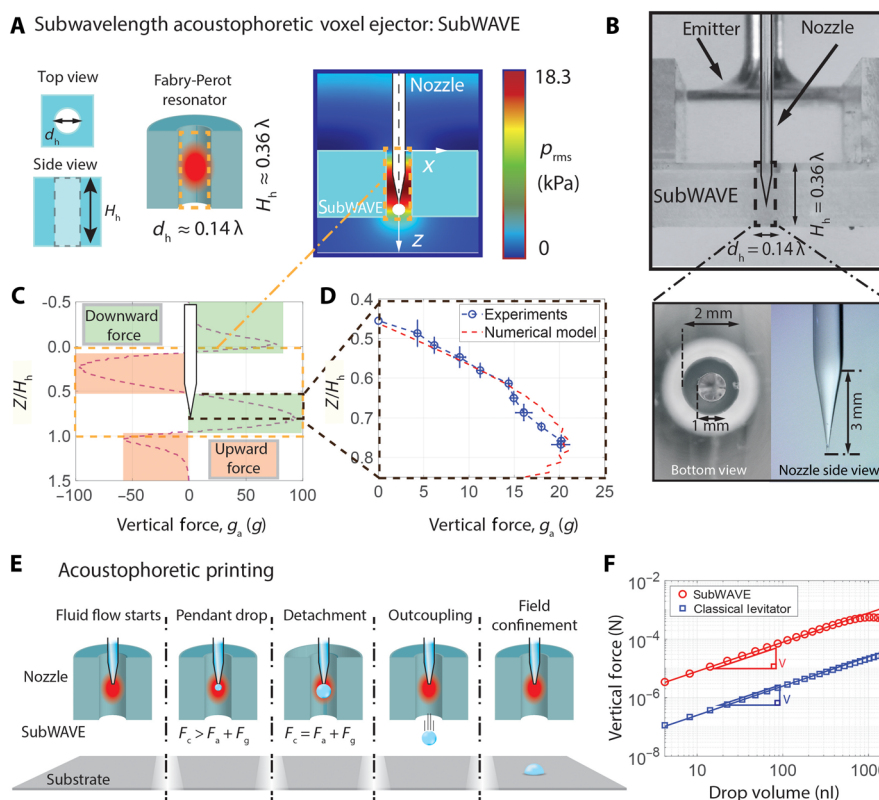


Fig. 2. Principle and acoustophoretic properties of the subWAVE. (A) Schematic view of the subwavelength acoustophoretic voxel ejector (left). The resonance (schematically shown in red) leads to high acoustic pressure amplification while keeping the field strongly confined (right). (B) Side view of the experimental setup (top) and close-up of the tapered nozzle ($\lambda \approx 14$ mm) (bottom). Calculated vertical force distribution inside the subWAVE (C) and its experimental validation (D). (E) Schematic illustration of acoustophoretic printing, which shows that when the total acoustophoretic and gravitational forces exceed the capillary force, droplet detachment and outcoupling from the subWAVE enable patterning on any substrate. (F) Log-log plot of vertical force generated within the subWAVE as a function of drop volume compared to a classical standing-wave levitator.

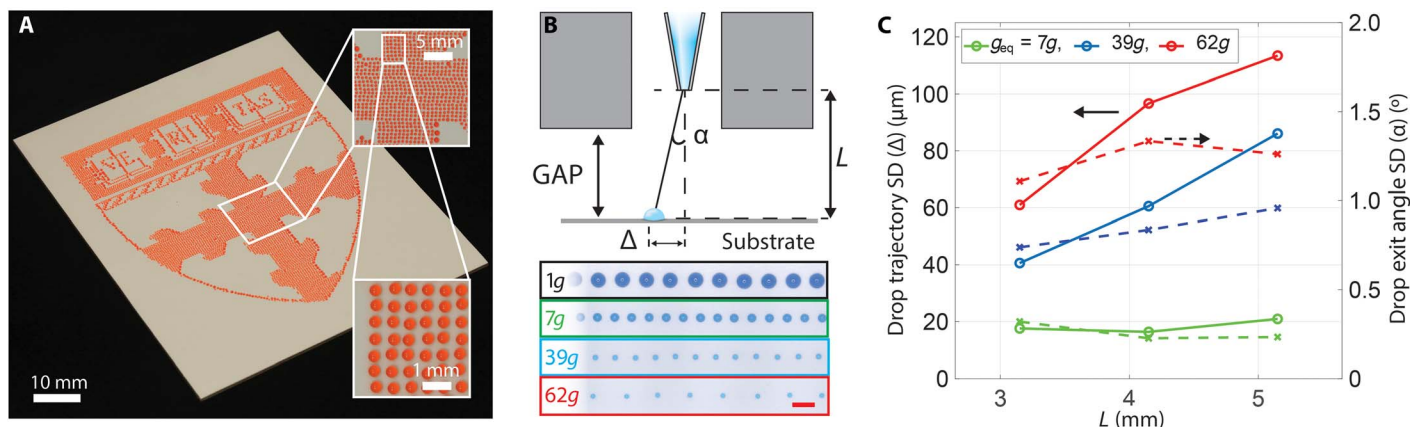


Fig. 3. Drop-on-demand acoustophoretic printing. (A) Drop-on-demand printing of a rasterized (large-area) image, in which fluid dispensing is synchronized with the substrate movement to provide spatial control over the patterned droplets. (B) Schematic view of droplet deposition (top) illustrating the exit angle α , drop trajectory Δ , distance L between the nozzle and substrate, and offset distance between subWAVE exit and substrate. Images of patterned droplet traces as a function of acoustophoretic pressure g_a . Scale bar, 2 mm. (C) Plot of positional accuracy of droplets deposited via acoustophoretic printing as a function of this offset distance L . The subWAVE can be placed as close as 1 mm (0.07λ) from the substrate without hindering the drop deposition process. (Note that the drop trajectory and exit angle are plotted as SDs.)

control and their proliferation over a 7-day period does not differ in a statistically significant manner from that observed for the drops produced by simple dripping (Fig. 4Db). After longer culture periods (day 17), we observed additional cell proliferation and spreading within the printed droplets (Fig. 4D). We also performed immunofluorescent

staining for common multipotency markers of hMSCs [CD105⁺/CD90⁺/CD45⁻; Fig. 4Dd and (38)], which suggests that the cells retain their multipotent state after acoustophoretic printing. Specifically, these cells stain positive for CD105 and CD90, but negative for CD45, akin to control cells cultured on plastic for the same duration in the same stem cell

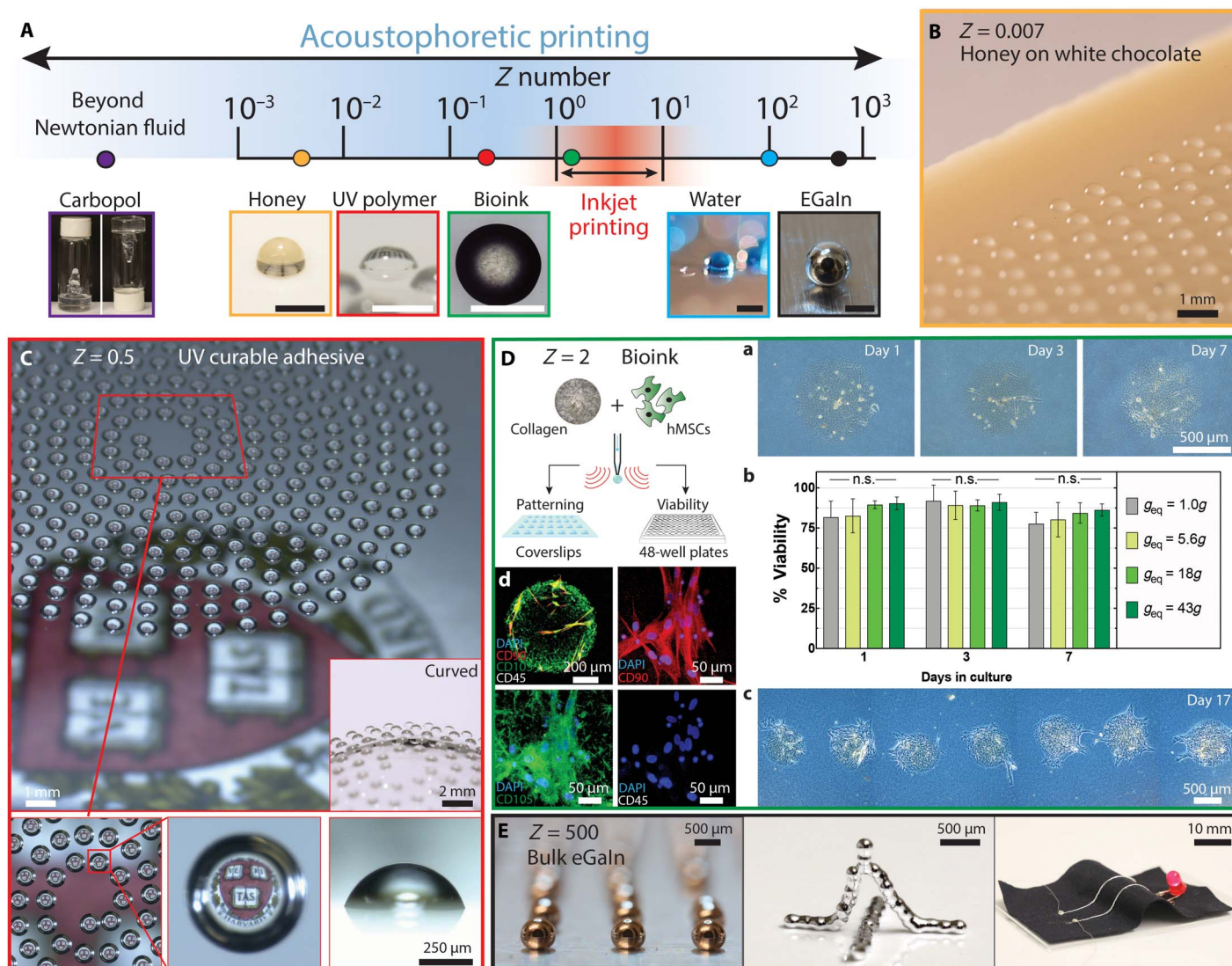


Fig. 4. Acoustophoretic printing of food, optical, biological, and electrically conductive materials. (A) Schematic illustration of the broad Z range enabled by acoustophoretic printing, which extends over nearly six orders of magnitude, and corresponding images of droplets patterned by this approach. Note that the typical Z range for inkjet printing is highlighted in red. Scale bars, 500 μ m. (B) Honey droplets printed on white chocolate. (C) Optical adhesive resin printed in a spiral motif yielding a microlens array. (D) Acoustophoretic printing of hMSC-laden collagen I ink for viability testing and patterning. (a) Bright-field images of printed droplets composed of hMSCs in a collagen I matrix ($g_{eq} = 43g$) cultured for 7 days. (b) Cell viability of acoustophoretically printed droplets with increasing acoustic force ($n = 6$). n.s., not significant. (c) Bright-field image of patterned droplets at day 17 ($g_{eq} = 18g$). (d) Representative confocal microscopy images of an immunofluorescently stained, printed droplet ($g_{eq} = 43g$) cultured to day 17 and a higher-magnification region stained for CD105 (green), CD90 (red), CD45 (gray), and nuclei [4',6-diamidino-2-phenylindole (DAPI), blue]. (E) Acoustophoretic printing of a liquid metal ink composed of eGaln patterned as individual droplets at room temperature in noncontact mode.

medium (Fig. 4D and fig. S7B). Thus, over the wide range of acoustophoretic forces applied during the patterning process, the printed hMSC-laden inks retain their cell viability and function.

As a final exemplar, we printed a liquid metal ink composed of eutectic gallium-indium (eGaln), which has a low viscosity ($\mu = 2$ mPa·s), high surface tension ($\sigma = 624$ mN/m), and high $Z = 500$. This material, which quickly forms a thin oxide shell upon contact with air, cannot be ejected as individual drops under ambient conditions in noncontact mode by other printing methods (39, 40). By contrast, individual liquid metal drops ($R \approx 300$ μ m) are generated via acoustophoretic printing at $g_a \approx 20g$. Using this method, we fabricated both self-supporting 3D eGaln

structures (Fig. 4E and movie S5) and conductive eGaln electrodes on stretchy textiles.

DISCUSSION

We have developed a new printing platform for droplet generation and patterning that harnesses acoustophoretic forces. By exploiting the nonlinear effects of a single subwavelength ultrasonic cavity, one can generate a well-controlled, highly localized acoustic pressure that enables monodisperse drop on demand printing of disparate materials that have an unprecedented range of physical properties. Our approach opens

new avenues for the digital fabrication of functional, structural, and biological materials in a voxel-by-voxel manner.

MATERIALS AND METHODS

Materials

Several materials were formulated into inks for acoustophoretic printing, including polymer solutions and gels, honey, a UV-curable optical adhesive, a cell-laden collagen solution, and a liquid metal. The polymer solutions were composed of 60 wt % PEG8000 (Sigma-Aldrich) or 50 wt % PEG10000 (Sigma-Aldrich) dissolved in deionized water. For PEG8000 solutions, a blue dye (IFWB-14, Riskfactor; 0.4 volume %) was added to enhance visualization. Each ink was mixed in a planetary mixer at 2350 rpm for 10 min. Polymer gels were produced by combining a cross-linked acrylic acid homopolymer (Carbopol C934) with deionized water in a planetary mixer at different concentrations. Honey and white chocolate were used as received. A UV-curable optical adhesive composed of NOA60 (Norland Inc.) was also used as received and housed in a 3-cm³ UV blocking syringe barrel (Nordson EFD) for printing. Biological inks were produced by suspending hMSCs (bone marrow-derived, RoosterBio) in a rat tail collagen type I solution (5 mg/ml) (stock, 9.61 mg/ml; Corning) at a concentration of 5×10^5 cells/ml at neutral pH. Before printing, this ink was kept on ice to prevent collagen gelation (see below). hMSCs were cultured according to the manufacturer's instructions in the RoosterBasal-MSC culture medium with the RoosterBooster supplement and were not used beyond third passage. Finally, eGaIn (5N Plus), composed of 75% gallium and 25% indium alloy, a liquid metal under ambient conditions, was loaded into a 3-cm³ syringe barrel (Nordson EFD) and used directly in our acoustophoretic printing system. The rheological properties of each of these materials were measured using a controlled stress rheometer (DHR-3, TA Instruments) equipped with a 40-mm-diameter, 2° cone and plate geometry.

Acoustophoretic printing

Our acoustophoretic printer consisted of a sound source, a subwavelength resonator, and a fluid dispensing system. A magnetostrictive transducer (Etrema C18A) excited the resonant mode of the custom-designed emitters at the resonance frequencies of 26.460 and 23.640 kHz. The subWAVE acoustic chamber was custom-designed and manufactured in the form of a rectangular chamber (15 mm × 65 mm × 7.5 mm) using Computer Numeric Control (CNC)-milled or 3D-printed (Aureus, EnvisionTEC) acrylic parts. To visualize droplet ejection at the nozzle tip, the subWAVE was manufactured out of a glass capillary (outer diameter, 2.4 mm; inner diameter, 2.0 mm; length, 5.3 mm; VitroCom CV2024).

The emitter was located at one end, while the subwavelength chamber was located at the other end (fig. S8A). The transducer was driven by a sinusoidal signal at the resonance frequency of the system and amplified to a maximum value of 115 V (Peavey CS4080). During acoustophoretic printing, the nozzle remained stationary, while the substrate was moved in the *x-y* plane (or also in the *z* direction, as needed). The acoustic field, which was generated in air, surrounded the pendant droplet. The acoustic field was always active—detachment occurred when the combined acoustophoretic and gravitation forces exceeded the capillary force. Each material (ink) was housed in a syringe barrel, mated with a Luer-lock connection or PEEK connector (IDEX Health & Science), and then ejected through the nozzle with a constant flow rate by using both positive displacement systems (Harvard Apparatus PHD ULTRA

and Nordson EFD Ultra 2800) and pressure-based dispensing systems (in-house built and Nordson Ultimius V). Ink droplets form at the exit of the tapered glass nozzles, which were manufactured in-house using a pipette puller (Sutter P-97). The nozzle tips were treated with a hydrophobic coating (silane or Fusso, Crystal Armor) to minimize wetting. To account for manufacturing variability associated with the glass-pulled nozzles, we measured the $V|_{F=F_g}$ (simple dripping mode) for a given flow rate and nozzle. This volume represents the reference to calculate $g_a = V|_{F=F_g} / V|_{F=F_a} - 1$. Droplets were visualized using a high-speed camera (Phantom V7.1 or Photron SA1.1).

To pattern droplets via acoustophoretic printing, the subWAVE printheads were mounted on either a Sherline 5430 or Shapeoko 3 (three-axis motion-controlled) stage. Rasterized pictures were printed using G-CODE generated from an in-house MATLAB R2016b script, while the 3D structures were printed using G-CODE generated by Slic3r.

Acoustophoretic printing throughput

A requisite condition for acoustophoretic printing was that drops formed via a simple dripping mode. Hence, during the time scale of interest for drop formation and detachment, the surface tension forces must exceed the inertial and viscous forces. For a low-viscosity fluid, the upper flow boundary can be defined by imposing a flow through the nozzle q that does not exceed the jetting limit (17), $q < \pi(d^3\sigma/2\rho)^{1/2}$, akin to droplet generation in coflowing microfluidic devices (Fig. 1B, right axis). As a first approximation, one can simply require that the capillary number $Ca = \mu \cdot \zeta / \sigma < 1$ for viscous fluids, with ζ being the fluid velocity at the nozzle exit. Upon increasing the fluid viscosity, the velocity ζ through the nozzle was constrained to an upper boundary. The lower the velocity ζ , the lower the flow rate q and the maximum ejection frequency for the same equivalent acoustophoretic force. Fluid viscosity limits the ejection process only at high throughput (fig. S2A). A simple dripping regime (7) was required for Eq. 1 to be valid. For viscosities between 1 and 100 mPa·s, the maximum ejection frequencies were limited by the inertial forces of the fluid compared to the surface tension forces (41), while at high viscosities (>100 mPa·s), the maximum ejection frequencies were limited by the viscous forces of the fluid compared to the surface tension forces.

Bioprinting hMSC-laden collagen I matrices

The hMSC-laden collagen ink was loaded into an ice-cold glass syringe (Hamilton 1005 TTL) and stored on ice until mounted onto the syringe pump, where it is at ~5°C (fig. S7A). The nozzle and substrate were held at ~8°C. To minimize water evaporation, the printing environment was maintained at 95% relative humidity, and patterned well plates were sealed with parafilm. Sterility was enhanced using air and water purifiers (fig. S7A).

To quantify cell viability, 20 μ l of the solution was printed into each well of a 48-well plate at a flow rate of 60 μ l/min. Six biological repeats per condition (that is, dripping mode, and $g_{eq} = 5.6g$, $g_{eq} = 18g$, and $g_{eq} = 43g$) and two controls (manually pipetted and simple dripping mode, $g_{eq} = 1g$) were prepared for a total of 24 wells per plate. Note that the hMSC viability within the ink reservoir begins to decline after 90 min (42); hence, all printing was carried out before this time. Upon printing, collagen I within each drop was gelled at 37°C, 5% CO₂, and 95% humidity in a cell culture incubator for 30 min. The printed and gelled drops were then covered with 300- μ l cell culture medium for subsequent culture (RoosterBio Basal medium with Booster supplement and 1% antibiotic/antimycotic solution; Corning). The medium was

changed every 48 hours. We carried out an MTS assay (Promega) on the printed drops and both controls at days 1, 3, and 7 after patterning. Briefly, we incubated the cell-laden droplets in 300 μl of cell culture medium supplemented with 60 μl of MTS assay reagent for 4 hours. Next, 150 μl of each culture supernatant was transferred into a 96-well plate, and cell viability was assessed by measuring the production of formazan through its absorbance at 490 nm. These data were processed in GraphPad Prism for statistical analysis. After subtracting the background value corresponding to the absorbance of a cell-free well, the individual values were normalized to the mean of the manually pipetted control ($g_{eq} = 1g$). We perform a one-way analysis of variance (ANOVA) with Tukey's multiple comparisons test to quantify differences in cell viability within droplets patterned by acoustophoretic printing at increasing g_{eq} , simple dripping, and manual pipetting, where all reported data were normalized to the manually pipetted control. A P value of below 0.01 is considered statistically significant for our experiments.

For patterning, drop visualization, and immunofluorescent staining, the hMSC-laden collagen I ink was deposited onto hydrophobically modified glass coverslips (Fusso, Crystal Armor) to ensure that the printed drops consisted of hemispherical features with a contact angle of roughly 90° . Coverslips were placed in six-well plates and printed at a nozzle-substrate distance of about 15 mm. After printing, collagen I within each drop was gelled at 37°C , 5% CO_2 , and 95% humidity in a cell culture incubator for 30 min and then carefully encapsulated in a secondary hydrogel in a 35-mm petri dish to avoid droplet detachment from the hydrophobic surface of the glass slide during subsequent cell culture. The secondary hydrogel was composed of 2 wt % porcine gelatin type A (Sigma), bovine fibrinogen (10 mg/ml) (Millipore), 0.2 wt % transglutaminase (Modernist Pantry), 2.5 mM calcium chloride (Macron Chemicals), and thrombin (1 U/ml) (MP Biomedicals) in phosphate-buffered saline (PBS) without calcium/magnesium (Corning), prepared as previously described (42). Upon deposition and gelation of the secondary hydrogel (15 min, 37°C), 2 ml of RoosterBio cell culture medium was added to each well and the cell-laden droplets were cultured for 3, 7, or 17 days with medium changes every 48 hours. During culture, the cells were imaged using an inverted Leica DM IL microscope with objectives ranging from $4\times$ to $10\times$. Following cell culture, hMSCs within each droplet were fixed in 10% buffered formalin for 30 min at room temperature. Subsequently, to assess multipotency marker expression, the cell-laden droplets were stained via immunofluorescence. Briefly, the samples were washed in PBS with calcium/magnesium for several hours after fixation and incubated with a blocking solution overnight at 4°C containing 1 wt % donkey serum in PBS with 0.125 wt % Triton X-100 to block nonspecific binding of the antibodies. To visualize surface marker expression, the samples were then incubated with primary antibodies directed against the marker of interest (table S1) in a staining solution containing 0.5 wt % bovine serum albumin and 0.125 wt % Triton X-100. Unbound primary antibody was washed out by three washing steps in PBS over the course of the day. Binding of the primary antibody was detected using a fluorophore-coupled secondary antibody directed against the primary antibody species. Secondary antibodies were incubated for 5 hours in staining solution at room temperature. Following the secondary antibodies, cell nuclei were counterstained via incubation of the samples in DAPI (KPL) (1 $\mu\text{g}/\text{ml}$) in staining solution. To remove unbound secondary antibodies and nonspecifically bound DAPI, the samples were washed again three times in PBS over the course of the day. Subsequently, the samples were imaged using an upright laser scanning confocal micro-

scope (Zeiss LSM 710) with water immersion objectives from $10\times$ to $40\times$ and spectral lasers at 405-, 488-, 561-, and 633-nm wavelengths. These images were processed using Imaris software (Bitplane) for 3D reconstruction and maximum intensity projection. All image processing was performed on all planes equally.

Printing accuracy

To determine the accuracy of acoustophoretic printing, droplets of a 1:1 water-glycerol mixture were patterned along a straight line on a Teflon-coated substrate. ImageJ software was used to define the centroid of each droplet, while MATLAB R2016b was used to perform a linear regression on the obtained coordinates. Increasing the nozzle-substrate distance L spreads the Gaussian distribution of the droplets along the centerline, confirming the ballistic nature of the printing process (fig. S5). The angle trajectory SD is in the range of 0.2° to 2° . These values are higher than those reported for inkjet printing (43), which can be as low as 0.2° for well-optimized inks printed on a desktop printer (for example, Fuji Dimatix). Using our first-generation subWAVE printhead, the positional variation was about 60 μm for the highest acoustophoretic field ($g_a = 62g$) used at a nozzle-substrate distance of $L = 3.15$ mm (Fig. 3C, left axis). At a driving frequency of about 25 kHz (wavelength $\lambda = 14$ mm), the imposed minimum $L = 3.15$ mm.

Analytical model

The acoustic force g_a is assumed to scale with the droplet volume, that is, $F_a \propto V$. Using the Rayleigh equation for the radiation pressure (29)

$$P_{\text{rad}} = \left(\frac{P_{\text{rms}}^2}{2\rho_f c^2} - \rho_f \frac{\text{Vel}_{\text{rms}}^2}{2} \right) \quad (2)$$

where ρ_f and c are the density and the sound speed of the acoustic medium, and P_{rms} and Vel_{rms} are the root mean square (rms) of acoustic pressure and acoustic particle velocity, respectively. It is possible to calculate the acoustic force by integrating P_{rad} around the sample surface S

$$F_a = \int_S P_{\text{rad}} \vec{n} dS \quad (3)$$

with \vec{n} being the normal component inward to S . This approach has been validated multiple times, both numerically and experimentally, when $\rho \gg \rho_f$ (29). Figure 2F shows the vertical acoustic force (along the z direction) acting on a rigid sphere pendant from a fixed nozzle diameter d of 10 μm for both a classical levitator (fig. S8, B to D) and our subWAVE. To compare the results, equivalent axisymmetric geometries were simulated for both systems. The same emitter-to-reflector distance ($H = 0.52 \lambda$) and emitter excitation (maximum oscillation velocity $v_{\text{max}} = 1$ m/s) were used. The reflector and emitter diameters are chosen to be 5λ to ensure that the results are independent of the width of the resonators and to approach a quasi-plane wave condition. Acoustic forces are linearly dependent on the drop volume V , confirming the R^3 scaling law. The small decrease in force calculated for $R > 500 \mu\text{m}$ was due to the increasing influence that the larger drops had on the acoustic field. When $R > 500 \mu\text{m}$, the droplet was large enough to occupy a cross-sectional area within the subWAVE (diameter of 2 mm), decreasing the acoustic pressure within it. Note that the center of the droplet changed along the z direction, because the position of the nozzle tip was fixed. However, as shown in Fig. 2F, this variation has a small influence on the $F_a \propto V$ scaling.

The second scaling relationship used in the model is $F_a \propto P^2$, which has also been numerically and experimentally verified for conventional acoustic levitators (15, 29). Figure S9A shows the validity of this scaling also for the presented subWAVE. The driving voltage, emitter oscillation amplitude, and acoustic pressure were considered linearly dependent (15). When the acoustic force acts on a pendant drop, the portion of the drop surface in contact with the nozzle orifice does not experience any acoustic pressure (Fig. 1A). This differs from the typical $F_a \propto VP^2$ scaling, which assumes the sample to be an unconstrained sphere, and so $R \gg d$. Figure S9B reveals that the nozzle size effect on the acoustic force is significant when $8R < d$, and it rapidly decreases to zero when $4R < d$. This numerical result suggests that for practical droplet ejection, the minimum droplet radius must exceed the external nozzle diameter akin to continuous inkjet (8).

An axisymmetric linear acoustic model is implemented using COMSOL Multiphysics 5.0 to calculate the acoustic field inside the subWAVE. The acoustic force is measured with both Gor'kov potential model and the surface integral of the radiation pressure on the sphere (29). For all simulations, a frequency of 25 kHz is used and the dimensions of the acoustic chamber are scaled with the wavelength. Figure 2 (C and D) shows the predicted acoustic force along the z axis of both the classical levitator and our subWAVE. In this specific context, the Gor'kov potential U has been used (15, 29). The potential and force expressions were valid as long as the assumption of a standing wave was respected and the spherical particle was much smaller than the wavelength λ of the acoustic field [in practical terms, $R < 0.1\lambda$ (29)]. Gor'kov did not consider multiple scattering effects on the sample, and his model was valid far from the wall of the acoustic chamber. Because of the limited dimension of the subWAVE, a pendant drop finds itself close to the side walls of the ejector (Fig. 2A). Nonetheless, Fig. 2F shows how the linear scaling of V is confirmed up to $V < 500$ nl (corresponding to $R < 500$ μm), validating the use of the Gor'kov potential for the subWAVE for the range of V of interest. The Gor'kov potential was able to predict the acoustic force acting on a sphere, whose center was the reference z coordinate. When measuring the force distribution along the subWAVE (Fig. 2D), it is the nozzle tip position inside the subWAVE that must be known. This z coordinate corresponded to the top of the sphere (pendant drop). To compare the experimental and numerical results, the position of the sphere (droplet) center was calculated by adding the radius R to the nozzle tip coordinate (fig. S9C). The radius R of the detached droplet was obtained for each case by image processing. In Fig. 2D, the vertical force amplitude calculated by the Gor'kov potential was normalized with respect to the maximum force obtained during the experiment. Because of measurement limitations, the integrated radiation pressure calculated by analytical models typically overestimated the magnitude of the acoustic levitation force (29).

SUPPLEMENTARY MATERIALS

Supplementary material for this article is available at <http://advances.sciencemag.org/cgi/content/full/4/8/eaat1659/DC1>

Materials and Methods

Supplementary Analysis

Fig. S1. Horizontal acoustophoretic printing of liquid droplets.

Fig. S2. Acoustophoretic printing of viscous fluids.

Fig. S3. The Fabry-Perot resonator.

Fig. S4. Acoustophoretic 3D printing of aqueous polymer solution.

Fig. S5. Droplet trajectory accuracy and distribution.

Fig. S6. Acoustophoretic printing of honey droplets.

Fig. S7. Acoustophoretic bioprinting.

Fig. S8. Classical acoustophoretic levitator.

Fig. S9. Scaling and nozzle effects on acoustophoretic forces.

Fig. S10. Pressure drop as function of nozzle diameter.

Table S1. Primary antibodies and markers of interest.

Movie S1. Acoustophoretic printing of liquids using different nozzle diameters d and equivalent accelerations g_{eq} .

Movie S2. Horizontal acoustophoretic printing of a 1:1 water-glycerol mixture.

Movie S3. Acoustophoretic printing of single droplet of honey compared to simple dripping.

Movie S4. Confocal z-stack movie and 3D renderings of acoustophoretically printed droplets composed of hMSCs suspended in a collagen I matrix.

Movie S5. Acoustophoretic printing of liquid metal droplets, in which 3D structures are assembled in a contact-free manner (real time).

REFERENCES AND NOTES

- R. L. Truby, J. A. Lewis, Printing soft matter in three dimensions. *Nature* **540**, 371–378 (2016).
- B. Derby, Inkjet printing of functional and structural materials: Fluid property requirements, feature stability, and resolution. *Annu. Rev. Mater. Res.* **40**, 395–414 (2010).
- M. Gruene, C. Unger, L. Koch, A. Deiwick, B. Chichkov, Dispensing pico to nanolitre of a natural hydrogel by laser-assisted bioprinting. *Biomed. Eng. Online* **10**, 19 (2011).
- Z. Zhang, R. Xiong, R. Mei, Y. Huang, D. B. Chrisey, Time-resolved imaging study of jetting dynamics during laser printing of viscoelastic alginate solutions. *Langmuir* **31**, 6447–6456 (2015).
- H. Yang, Y. He, C. Tuck, R. Wildman, R. Hague, High viscosity jetting system for 3D reactive inkjet printing, in *Twenty Forth Annual International Solid Freeform Fabrication Symposium—An Additive Manufacturing Conference*, Austin, TX, 12 to 14 August 2013, pp. 505–513.
- M. S. Brown, C. F. Brasz, Y. Ventikos, C. B. Arnold, Impulsively actuated jets from thin liquid films for high-resolution printing applications. *J. Fluid Mech.* **709**, 341–370 (2012).
- C. Clanet, J. C. Lasheras, Transition from dripping to jetting. *J. Fluid Mech.* **383**, 307–326 (1999).
- O. A. Basaran, Small-scale free surface flows with breakup: Drop formation and emerging applications. *AIChE J.* **48**, 1842–1848 (2002).
- R. Edgeworth, B. J. Dalton, T. Parnell, The pitch drop experiment. *Eur. J. Phys.* **5**, 198–200 (1984).
- J.-U. Park, M. Hardy, S. J. Kang, K. Barton, K. Adair, D. K. Mukhopadhyay, C. Y. Lee, M. S. Strano, A. G. Alleyne, J. G. Georgiadis, P. M. Ferreira, J. A. Rogers, High-resolution electrohydrodynamic jet printing. *Nat. Mater.* **6**, 782–789 (2007).
- P. Galliker, J. Schneider, H. Eghlidi, S. Kress, V. Sandoghdar, D. Poulikakos, Direct printing of nanostructures by electrostatic autofocussing of ink nanodroplets. *Nat. Commun.* **3**, 890 (2012).
- A. Marzo, S. A. Seah, B. W. Drinkwater, D. R. Sahoo, B. Long, S. Subramanian, Holographic acoustic elements for manipulation of levitated objects. *Nat. Commun.* **6**, 8661 (2015).
- K. Melde, A. G. Mark, T. Qiu, P. Fischer, Holograms for acoustics. *Nature* **537**, 518–522 (2016).
- D. Baresch, J.-L. Thomas, R. Marchiano, Observation of a single-beam gradient force acoustical trap for elastic particles: Acoustical tweezers. *Phys. Rev. Lett.* **116**, 024301 (2016).
- D. Foresti, M. Nabavi, M. Klingauf, A. Ferrari, D. Poulikakos, Acoustophoretic contactless transport and handling of matter in air. *Proc. Natl. Acad. Sci. U.S.A.* **110**, 12549–12554 (2013).
- I. Leibacher, J. Schoendube, J. Dual, R. Zengerle, P. Koltay, Enhanced single-cell printing by acoustophoretic cell focusing. *Biocircuits* **9**, 024109 (2015).
- L. Tian, N. Martin, P. G. Bassindale, A. J. Patil, M. Li, A. Barnes, B. W. Drinkwater, S. Mann, Spontaneous assembly of chemically encoded two-dimensional coacervate droplet arrays by acoustic wave patterning. *Nat. Commun.* **7**, 13068 (2016).
- T. M. Llewellyn-Jones, B. W. Drinkwater, R. S. Trask, 3D printed components with ultrasonically arranged microscale structure. *Smart Mater. Struct.* **25**, 02LT01 (2016).
- B. Hadimioglu, S. A. Elrod, D. L. Steinmetz, M. Lim, J. C. Zesch, B. T. Khuri-Yakub, E. G. Rawson, C. F. Quate, Acoustic ink printing. *IEEE Ultrason. Symp. Proc.* **12**, 929–935 (1992).
- F. D. Fuller, S. Gul, R. Chatterjee, E. S. Burgie, I. D. Young, H. Lebrette, V. Srinivas, A. S. Brewster, T. Michels-Clark, J. A. Clinger, B. Andi, M. Ibrahim, E. Pastor, C. De Lichtenberg, R. Hussein, C. J. Pollock, M. Zhang, C. A. Stan, T. Kroll, T. Fransson, C. Weninger, M. Kubin, P. Aller, L. Lassalle, P. Bräuer, M. D. Miller, M. Amin, S. Korodov, C. G. Roessler, M. Allaire, R. G. Sierra, P. T. Docker, J. M. Glownia, S. Nelson, J. E. Koglin, D. Zhu, M. Chollet, S. Song, H. Lemke, M. Liang, D. Sokaras, R. Alonso-Mori, A. Zouni, J. Messinger, U. Bergmann, A. K. Boal, J. M. Bollinger, C. Krebs, M. Högbom, G. N. Phillips, Drop-on-demand sample delivery for studying biocatalysts in action at X-ray free-electron lasers. *Nat. Methods* **14**, 443–449 (2017).
- D. J. Collins, T. Alan, K. Helmerston, A. Neild, Surface acoustic waves for on-demand production of picoliter droplets and particle encapsulation. *Lab Chip* **13**, 3225–3231 (2013).

22. H. Tanaka, Y. Wada, Y. Mizuno, K. Nakamura, Effect of holed reflector on acoustic radiation force in noncontact ultrasonic dispensing of small droplets. *Jpn. J. Appl. Phys.* **55**, 067302 (2016).
23. M. K. Tan, J. R. Friend, L. Y. Yeo, Interfacial jetting phenomena induced by focused surface vibrations. *Phys. Rev. Lett.* **103**, 024501 (2009).
24. J. O. Castro, S. Ramesan, A. R. Rezk, L. Y. Yeo, Continuous tuneable droplet ejection via pulsed surface acoustic wave jetting. *Soft Matter* **14**, 5721–5727 (2018).
25. J. Christensen, L. Martin-Moreno, F. J. Garcia-Vidal, Theory of resonant acoustic transmission through subwavelength apertures. *Phys. Rev. Lett.* **101**, 014301 (2008).
26. J. Zhu, J. Christensen, J. Jung, L. Martin-Moreno, X. Yin, L. Fok, X. Zhang, F. J. Garcia-Vidal, A holey-structured metamaterial for acoustic deep-subwavelength imaging. *Nat. Phys.* **7**, 52–55 (2011).
27. S. A. Cummer, J. Christensen, A. Alù, Controlling sound with acoustic metamaterials. *Nat. Rev. Mater.* **1**, 16001 (2016).
28. C. Wang, F. Cai, F. Li, L. Meng, Y. Kang, H. Zheng, Acoustic manipulation of microparticles in a sub-wavelength slot between two plates. *IEEE Int. Ultrason. Symp.*, 1–3 (2016).
29. D. Foresti, M. Nabavi, D. Poulikakos, On the acoustic levitation stability behaviour of spherical and ellipsoidal particles. *J. Fluid Mech.* **709**, 581–592 (2012).
30. K. J. Mysels, Surface tension of solutions of pure sodium dodecyl sulfate. *Langmuir* **2**, 423–428 (1986).
31. D. Foresti, M. Nabavi, D. Poulikakos, Contactless transport of matter in the first five resonance modes of a line-focused acoustic manipulator. *J. Acoust. Soc. Am.* **131**, 1029–1038 (2012).
32. C. Devendran, D. R. Billson, D. A. Hutchins, A. Neild, Optimisation of an acoustic resonator for particle manipulation in air. *Sens. Actuators B Chem.* **224**, 529–538 (2016).
33. L. Li, A. Y. Yi, Development of a 3D artificial compound eye. *Opt. Express* **18**, 18125–18137 (2010).
34. I. T. Ozbolat, M. Hospodiuk, Current advances and future perspectives in extrusion-based bioprinting. *Biomaterials* **76**, 321–343 (2016).
35. H. Gudapati, M. Dey, I. T. Ozbolat, A comprehensive review on droplet-based bioprinting: Past, present and future. *Biomaterials* **102**, 20–42 (2016).
36. S. Moon, S. K. Hasan, Y. S. Song, F. Xu, H. O. Keles, F. Manzur, S. Mikkilineni, J. W. Hong, J. Nagatomi, E. Haeggstrom, A. Khademhosseini, U. Demirci, Layer by layer three-dimensional tissue epitaxy by cell-laden hydrogel droplets. *Tissue Eng. Part C Methods* **16**, 157–166 (2010).
37. T. Boland, V. Mironov, A. Gutowska, E. A. Roth, R. R. Markwald, Cell and organ printing 2: Fusion of cell aggregates in three-dimensional gels. *Anat. Rec. A Discov. Mol. Cell. Evol. Biol.* **272**, 497–502 (2003).
38. M. C. Schlegel, K.-J. Wenzel, A. Sarfraz, U. Panne, F. Emmerling, A wall-free climate unit for acoustic levitators. *Rev. Sci. Instrum.* **83**, 055101 (2012).
39. C. Ladd, J.-H. So, J. Muth, M. D. Dickey, 3D printing of free standing liquid metal microstructures. *Adv. Mater.* **25**, 5081–5085 (2013).
40. G. Li, X. Wua, D.-W. Lee, A galinstan-based inkjet printing system for highly stretchable electronics with self-healing capability. *Lab Chip* **16**, 1366–1373 (2016).
41. P. B. Umbanhowar, V. Prasad, D. A. Weitz, Monodisperse emulsion generation via drop break off in a coflowing stream. *Langmuir* **16**, 347–351 (2000).
42. D. B. Kolesky, K. A. Homan, M. A. Skylar-Scott, J. A. Lewis, Three-dimensional bioprinting of thick vascularized tissues. *Proc. Natl. Acad. Sci. U.S.A.* **113**, 3179–3184 (2016).
43. S. Haferl, D. Poulikakos, Experimental investigation of the transient impact fluid dynamics and solidification of a molten microdroplet pile-up. *Int. J. Heat Mass Transf.* **46**, 535–550 (2003).

Acknowledgments: We thank D. Kolesky, R. Weeks, Sophia Henze, and A. Kurum for their experimental assistance and M. Tiwari and M. T. Lis for discussions. **Funding:** This work was supported by the Society in Science through the Branco Weiss Fellowship and the NSF (grant no. DMR-1420570) through the Harvard Materials Research Science and Engineering Center. We also acknowledge the GETTYLAB for their generous donation in support of our research and support from the Blavatnik Biomedical Accelerator program. **Author contributions:** D.F. conceived the concept. D.F. and J.A.L. designed the research. D.F. performed all the experiments and developed the theoretical and numerical models. D.F., K.A.H., and K.T.K. designed and carried out the bioprinting experiments. D.F. and R.A. designed and carried out the experiments on the vertical force distribution, yield stress material voxel ejection, and printing precision. D.F. and F.S. designed and carried out the 3D printing experiment. D.F., D.P., and J.A.L. analyzed the data and wrote the manuscript. **Competing interests:** D.F., D.P., and J.A.L. have filed patents on this technology. D.F. and D.P. are inventors on a pending patent (U.S. patent no. 20170001439 A1, awarded on 30 January 2018; EU patent no. 15701957.1-1701). D.F. and J.A.L. are inventors on two additional patents (PCT/US17/43539, filed on 24 July 2017, and a U.S. provisional application no. 62664467, filed on 30 April 2018). K.A.H. is the cofounder and chief executive officer of NanoHybrids. D.P. is the cofounder of SCRONA and Hylomorph. J.A.L. is the cofounder of Voxell8, a multimaterial 3D printing company, and Electroninks, a printed electronics company. The authors declare no other competing interests. **Data and materials availability:** All data needed to evaluate the conclusions in the paper are present in the paper and/or the Supplementary Materials. Additional data related to this paper may be requested from authors.

Submitted 30 January 2018

Accepted 23 July 2018

Published 31 August 2018

10.1126/sciadv.aat1659

Citation: D. Foresti, K. T. Kroll, R. Amisshah, F. Sillani, K. A. Homan, D. Poulikakos, J. A. Lewis, Acoustophoretic printing. *Sci. Adv.* **4**, eaat1659 (2018).

Acoustophoretic printing

Daniele Foresti, Katharina T. Kroll, Robert Amissah, Francesco Sillani, Kimberly A. Homan, Dimos Poulikakos and Jennifer A. Lewis

Sci Adv 4 (8), eaat1659.
DOI: 10.1126/sciadv.aat1659

ARTICLE TOOLS

<http://advances.sciencemag.org/content/4/8/eaat1659>

SUPPLEMENTARY MATERIALS

<http://advances.sciencemag.org/content/suppl/2018/08/27/4.8.eaat1659.DC1>

REFERENCES

This article cites 41 articles, 2 of which you can access for free
<http://advances.sciencemag.org/content/4/8/eaat1659#BIBL>

PERMISSIONS

<http://www.sciencemag.org/help/reprints-and-permissions>

Use of this article is subject to the [Terms of Service](#)